

---

# NODE-ELEMENT HYPERGRAPH MESSAGE PASSING FOR FLUID DYNAMICS SIMULATIONS

---

**Rui Gao, Indu Kant Deo, Rajeev K. Jaiman**

Department of Mechanical Engineering

University of British Columbia

Vancouver, BC

{garrygao, indukant, rjaiman}@mail.ubc.ca

## ABSTRACT

A recent trend in deep learning research features the application of graph neural networks for mesh-based continuum mechanics simulations. Most of these frameworks operate on graphs in which each edge connects two nodes. Inspired by the data connectivity in the finite element method, we connect the nodes by elements rather than edges, effectively forming a hypergraph. We implement a message-passing network on such a node-element hypergraph and explore the capability of the network for the modeling of fluid flow. The network is tested on two common benchmark problems, namely the fluid flow around a circular cylinder and airfoil configurations. The results show that such a message-passing network defined on the node-element hypergraph is able to generate more stable and accurate temporal roll-out predictions compared to the baseline generalized message-passing network defined on a normal graph. Along with adjustments in activation function and training loss, we expect this work to set a new strong baseline for future explorations of mesh-based fluid simulations with graph neural networks.

## 1 Introduction

Deep neural networks defined on a graph data structure [1] are becoming increasingly popular in a wide range of applications [2, 3], including but not limited to citation networks, social networks, molecular science, etc. Embedded with the relational inductive bias between inter-connected entities [4], graph neural networks (GNN) have a great potential for learning physics-driven dynamics. Recently, GNNs have been introduced to the field of continuum mechanics [5, 6]. Recent works include the modeling of solid systems [7, 8, 9], fluid systems [10, 11, 12], as well as the interactions between them [13].

Traditional computational mechanics approaches of continuum systems, including computational fluid dynamics (CFD) and computational solid mechanics, usually discretize the simulation domain into a mesh. It turns out that such a mesh (Fig. 1a) can be converted to a graph  $\mathcal{G} = (\mathcal{V}, \mathcal{E})$  with nodes  $\mathcal{V}$  connected by edges  $\mathcal{E}$  rather easily. One can consider two approaches for the conversion of a mesh into a graph data structure. One approach (Fig. 1b) converts each vertex of the mesh to a node, and each cell boundary between two vertices to two directed edges. The other approach (Fig. 1c) converts each cell within the mesh into a node, while each border between two neighboring cells is converted to two directed edges.

With the system states originally attached to the mesh converted and re-attached to the graph as the node and edge features, a graph neural network can be applied to the converted graph to learn the temporal evolution of these features, effectively serving as a surrogate to the traditional CFD/CSM model of the system. For a graph neural network that fits into the generalized graph message-passing [4, 14] framework, each message-passing layer or step can be written as the combination of an edge update stage

$$e'_{ij} = \phi^e(e_{ij}, v_i, v_j), \quad (1a)$$

and a node update stage,

$$v'_i = \phi^v(v_i, \text{AGG}_j e'_{ji}), \quad (1b)$$

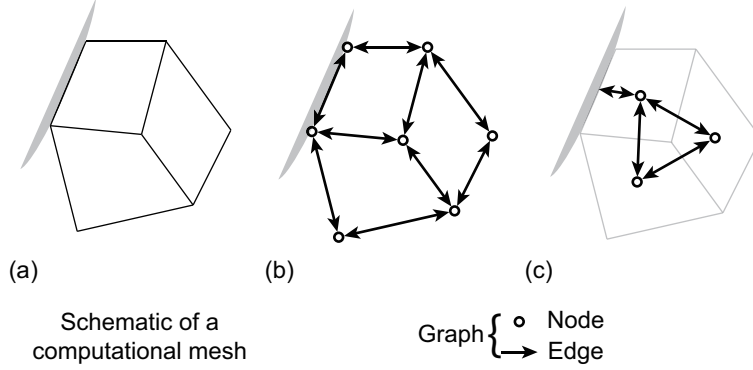


Figure 1: Conversion of a computational mesh to graph (a) Schematic representing a portion of computational mesh, (b)-(c) Two possible approaches to convert the mesh to a graph.

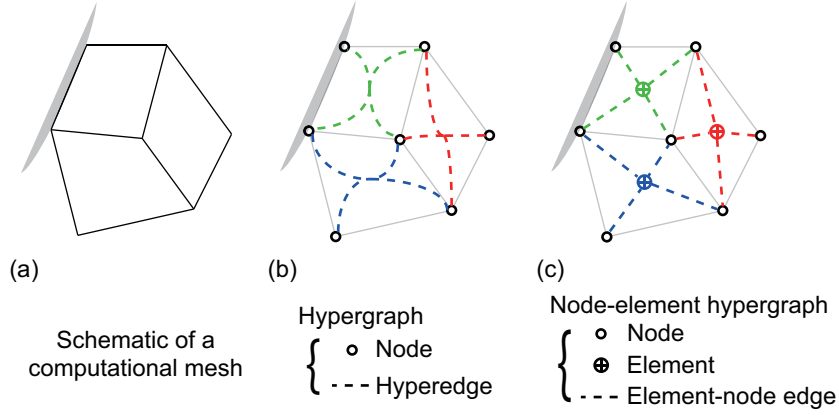


Figure 2: Conversion of a computational mesh to hypergraph (a) Schematic representing a portion of computational mesh, (b) Converted hypergraph, (c) Converted node-element hypergraph, adopted in this work.

in which  $v_i$  and  $v_j$  denote the node features attached to the nodes  $i$  and  $j$  respectively,  $e_{ij}$  denotes the edge feature attached to the directed edge pointing from node  $i$  to node  $j$ , and the superscript  $(\cdot)'$  denotes the updated features. The edge update function  $\phi^e$  and the node update function  $\phi^v$  are some nonlinear functions, e.g., multi-layer perceptrons. The function AGG is a permutation-invariant aggregation function that aggregates the information from all the edges pointing to each node  $i$ .

From a computational mechanics point of view, such a message-passing network defined on the graph  $\mathcal{G}$  mimics the finite volume method. Interpreting each node as a control volume, and each edge as the boundary between neighboring control volumes, the edge update function  $\phi^e$  calculates the "flux" of information between the two control volumes, and the node update function  $\phi^v$  evaluates the information in the control volume based on the aggregated incoming "flux". With a residual link for node and edge features, each layer or step within the message-passing network can be explained as one iteration in the iterative approximation to the ground truth flux and cell information updates, which are usually calculated by solving a linear system in the finite volume method.

Besides the finite volume method, many other approaches are available in computational mechanics. Another popular approach, the finite element method, treats each cell within the mesh as an *element* connecting all its vertices. In the assembly of the local stiffness matrices and load vectors, the vertices connected by each element interact with each other. Inspired by this data connectivity and this computational pattern, we connect the nodes  $\mathcal{V}$  by elements  $\mathcal{E}^+$ , effectively forming a hypergraph, illustrated in Fig. 2b. Further modifications of the hypergraph (detailed in Sec. 3.1) lead to a node-element hypergraph (Fig. 2c).

We implement a message-passing network that is defined on the node-element hypergraph converted from a mesh. The results from such a network are compared with that of the baseline generalized message-passing network [4, 6] defined on a normal graph converted from the same mesh. Experiments are performed on two fluid systems, namely the flow around a cylinder and the flow around an airfoil. Results show that our message-passing network defined on the

node-element hypergraph can generate more stable and accurate predictions than the baseline defined on the normal graph. With additional adjustments in the activation function and loss function, we develop an improved baseline for future explorations.

The remaining part of this paper is organized as follows: Section 2 contains the discussion on the existing works that are closely related to this paper. We then present the numerical background and formulations of the node-element graph and node-element graph message-passing networks in Sec. 3. The experiments and results are reported and discussed in Sec. 4. We conclude the work in Sec. 5.

## 2 Related works

**GNN for physics simulations** Graph neural network has been applied to the simulations of systems governed by physics laws for several years. The first applications focus on Lagrangian systems, like mass-spring systems [15] or fluid systems in which the continuous fluid flow is abstracted as moving particles [16]. More recently, it is introduced to the field of continuum mechanics [5, 6], inspiring a surge of works in the past two years. In particular, the encode-process-decode architecture with generalized graph message-passing layers [4, 6, 14] see popularity in many applications. Various techniques have been built above such an architecture, including field super-resolution [10], multi-grid methods [11, 12, 17, 18], physical invariances and/or equivariances [11], among many more.

**FEM-Inspired GNN applications** Several existing works have already taken some inspiration from finite element methods. Alet et al. [19], for example, constructs encoders and decoders that interpolate between data at random points within the field and data on the nodes of the graph, mimicking the behavior of shape function-based interpolation within the element in finite element methods. More recently, a few works start to use finite-element concepts to calculate the loss during the training process. Gao et al. [20], for example, proposed to calculate the loss by integrating the prediction error over the simulation domain using Gaussian quadrature integration with high-order shape functions instead of the traditional mean-squared loss on nodes.

Perhaps the most closely-related work to this research is the recent work by Lienen and Günnemann [21], who use a hypergraph message-passing step to estimate the time derivatives of features at different time instants, which are then sent to an ODE solver to generate predictions of the features. Different from their approach, we choose to follow an approach more similar to that of Pfaff et al. [6]: We stick to discrete time stepping with fixed intervals, the model is trained with one-step supervision only, and the model directly predict the difference of system states between neighboring time steps in a feed-forward manner rather than relying on an ODE solver. We also target generating stable and accurate predictions for a long period of time – up to more than thousand time steps, while the results reported by Lienen and Günnemann focus on predictions within a short period of future – 60 time steps at most.

## 3 Methodology

In this section, we describe the node-element hypergraph and the message-passing network defined on it. As the experiments reported in Sec. 4 are all 2D cases, we assume a 2D spatial domain for simplicity.

### 3.1 Node-element hypergraph

Consider a bounded spatial domain that is meshed. The mesh can be converted to an undirected hypergraph (Fig. 2b) by converting each vertex within the mesh to a node and each cell within the mesh to an undirected hyperedge connecting all vertices of the cell. Further instantiating each hyperedge as an undirected "element", and explicitly defining the connection between each element and each of the nodes it connects as an undirected element-node edge, we arrive at a node-element hypergraph  $\mathcal{G} = (\mathcal{V}, \mathcal{E}^+, \mathcal{E}_v)$  illustrated in (Fig. 2c), in which  $\mathcal{V}$  is the set of all nodes,  $\mathcal{E}^+$  is the set of all elements, and  $\mathcal{E}_v$  is the set of all element-node edges.

It should be mentioned that it is possible to adopt a directed hypergraph rather than an undirected version. Ma et al. [22], for example, used a directed hypergraph for the simulation of particulate suspensions. However, to achieve permutation invariance by covering all possible permutations, each undirected hyperedge connecting  $k$  nodes has to be converted to  $k!$  directed hyperedges. This means that the computational cost can be prohibitively high when each hyperedge is connecting more than three nodes (e.g., hypergraphs converted from quadrilateral or hexagonal meshes in 2D, or hypergraphs converted from meshes in 3D). Thus, we choose to stick to an undirected hypergraph in this work.

### 3.2 Node-element hypergraph message-passing

With the node-element hypergraph defined, we proceed to define the message-passing network on such a hypergraph. Similar to the generalized message-passing defined on a normal graph, one can define each message-passing layer or step on a node-element hypergraph as two consecutive stages, namely the element update stage and the node update stage. For the sake of consistency and simplicity in symbols, we write the equations in this subsection assuming a node-element hypergraph converted from the 2D quadrilateral mesh (with the conversion illustrated in Fig. 2).

For an element connecting four nodes  $i, j, k$  and  $l$  with node features  $v_i, v_j, v_k$ , and  $v_l$  respectively, we can write the element update stage in a general form,

$$e'_\square = \phi^{e,e} \left( e_\square, \text{AGG}_q^e \left( a_q \phi^{e,v} (v_q, e_\square, e_{\square,q}) \right) \right), \quad (2a)$$

in which  $e_\square$  is the element feature,  $e_{\square,q}$  is the feature carried by the element-node edge between element  $\square$  and node  $q$ ,  $q = i, j, k, l$ ,  $a_q$  is the attention weight,  $\text{AGG}^e$  denotes a permutation-invariant node aggregation function, and  $\phi^{e,v}$  and  $\phi^{e,e}$  are two functions that are preferably non-linear.

The subsequent node updating stage, in a similar level of generality, can be defined as

$$v'_i = \phi^{v,v} \left( v_i, \text{AGG}_\square^v \left( a_i \phi^{v,e} (v_i, e'_{i\square}, e_{i\square,i}) \right) \right), \quad (2b)$$

in which  $e_{i\square}$  denotes the element feature of any element that connects node  $i$  with some other nodes,  $e_{i\square,i}$  denotes the corresponding element-node feature for node  $i$  within such an element, and  $\phi^{v,e}$  and  $\phi^{v,v}$  are two functions that are preferably non-linear. Similar to the element update step, the node aggregation function  $\text{AGG}^v$  is also permutation-invariant.

In practice, these two update stages can be simplified significantly. In the experiments described in Sec. 4, we adopt simplified element update stage

$$e'_\square = \text{AGG}_q^e \left( \phi^e (v_q, e_\square, e_{\square,q}) \right). \quad (3a)$$

The node update stage, in a similar way, can be simplified to

$$v'_i = \text{AGG}_\square^v \left( \phi^v (v_i, e'_{i\square}, e_{i\square,i}) \right), \quad (3b)$$

or even more simply

$$v'_i = \phi^v (v_i, \text{AGG}_\square^v (e'_{i\square})), \quad (3c)$$

which reduces the computational overhead to a level comparable to the generalized message-passing network defined in Eq. 1, and also relatively easy to implement using a gather-scatter scheme similar to that in PyTorch Geometric [23]. An illustration of the two hypergraph message-passing stages described in Eq. 3 is described in Fig. 3.

### 3.3 Model architecture

In general, we follow the same encode-process-decode architecture and the forward Euler time stepping adopted in the MeshGraphNet baseline [6]. At roll-out time step  $t_n$ , the neural network output  $\hat{\psi}_n$  is added to the state parameters  $s_n$  to generate the predicted state parameters  $\hat{s}_{n+1}$  for time step  $t_{n+1}$ ,

$$s_{n+1} \approx \hat{s}_{n+1} = s_n + \hat{\psi}_n. \quad (4)$$

The neural network itself includes an encoder, a series of message-passing layers, and a decoder, stacked together in a feedforward fashion. The encoder, decoder, and the nonlinear functions in the message-passing layers are selected to be multi-layer perceptrons to be consistent with the baseline, but it should be noted that other choices are also possible. The model architecture is summarized in Fig. 4.

### 3.4 Choice of activation function

Most of the existing works discussed in Sec. 2 use Rectified linear Units (ReLU) or ReLU-like activation functions. We notice that the use of the sinusoidal activation function [24] improves the accuracy and smoothness of the captured details compared to ReLU in shape representation tasks. It is therefore reasonable to hypothesize that it should also help in capturing smooth and accurate system dynamics when used as the activation function for the encoder, decoder, and the nonlinear functions in the message-passing layers in the graph neural network. In Sec. 4, we report the results for both when ReLU-like activation functions are used, and when sinusoidal activation functions are used.

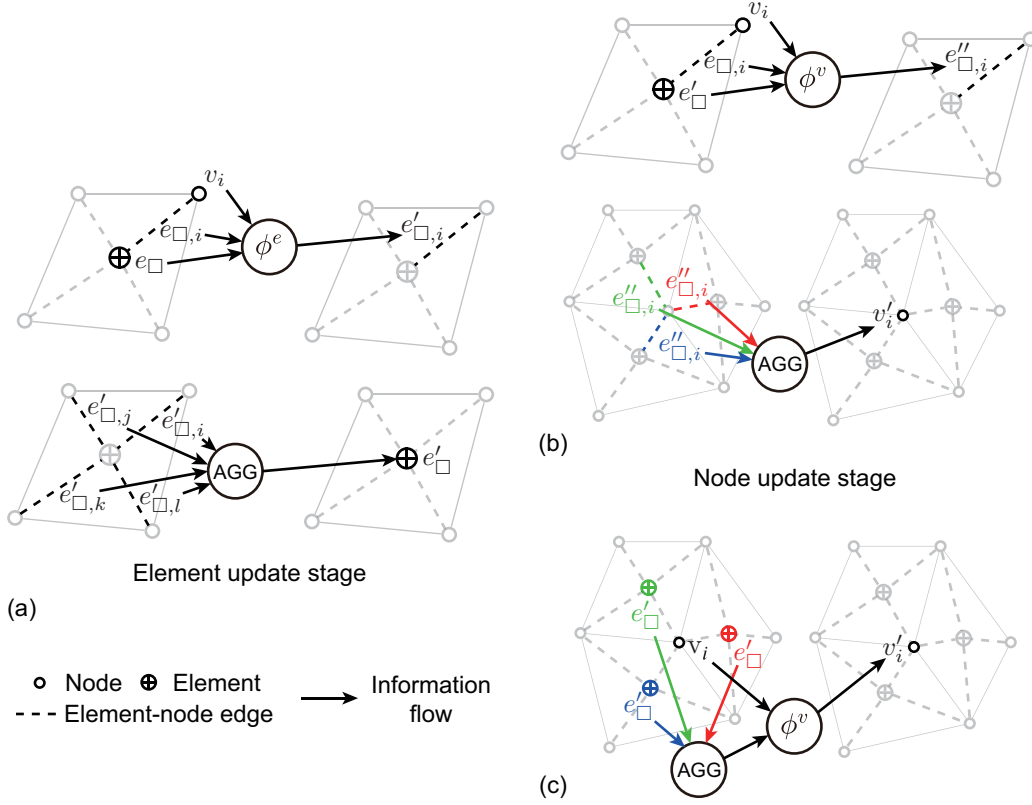


Figure 3: Schematic of the element and node update stages within each node-element hypergraph message-passing layer or step. (a) Element update stage (b) Node update stage described by Eq. 3b (c) Node update stage described by Eq. 3c.

### 3.5 Adaptive smooth $L_1$ loss

Most of the existing works discussed in Sec. 2 adopt mean squared error (MSE) as the training loss. When training the message-passing networks with sinusoidal activation functions, however, we observe that the use of MSE loss may lead to instability in the training process. We therefore seek an alternative training loss. Another typical loss, the  $L_1$  loss, might not be preferable in this case since it is not smooth at zero, and we thus adopt a smooth  $L_1$  loss [25] function, which states that for ground truth  $\psi$  and its neural network prediction  $\hat{\psi}$ , the loss

$$L_i(\psi_i, \hat{\psi}_i) = \begin{cases} (\psi_i - \hat{\psi}_i)^2 / 2\beta, & \text{if } |\psi_i - \hat{\psi}_i| < \beta \\ |\psi_i - \hat{\psi}_i| - \beta/2, & \text{if } |\psi_i - \hat{\psi}_i| \geq \beta \end{cases} \quad (5)$$

in which  $\beta$  is a non-negative parameter that controls the transition point between the  $L_2$  loss region and the  $L_1$  loss region. The subscript  $(\cdot)_i$  here denotes entry-by-entry calculation. A fixed  $\beta$  value is not preferable, since the loss function is not very different from the  $L_1$  loss when  $\beta$  is too small and will converge to a scaled  $L_2$  loss during training when  $\beta$  is too large. For the present case, the instability in training occurs when the training MSE error is relatively low, so an adaptive scheme for  $\beta$  is preferred. Assuming that the distribution of error during the training (approximately) follows a symmetric distribution centered at zero, the target is to make sure that the two tails of the distribution fall into the  $L_1$  loss region so that they do not lead to instability. More complex on-the-fly  $\beta$  adaptation algorithms like references [26, 27, 28] exist, but we choose to control it in this work using a simpler approach by setting  $\beta^2$  as the variance of the model prediction error

$$\beta^2 = \text{Var}(\psi - \hat{\psi}) \approx \text{MSE}(\psi_{\text{train}} - \hat{\psi}_{\text{train}}) \quad (6)$$

based on the idea that at least part of the two tails of any zero-centered symmetric distribution would reside more than one standard deviation away from zero. The variance of prediction error is approximated by computing the mean-squared error between the predicted and ground truth value of the whole training set, which can be further approximated on-the-fly by an exponential moving average

$$\beta^2 \leftarrow (1 - \frac{1}{N_b})\beta^2 + \frac{1}{N_b} \text{MSE}(\psi_{\text{batch}} - \hat{\psi}_{\text{batch}}) \quad (7)$$

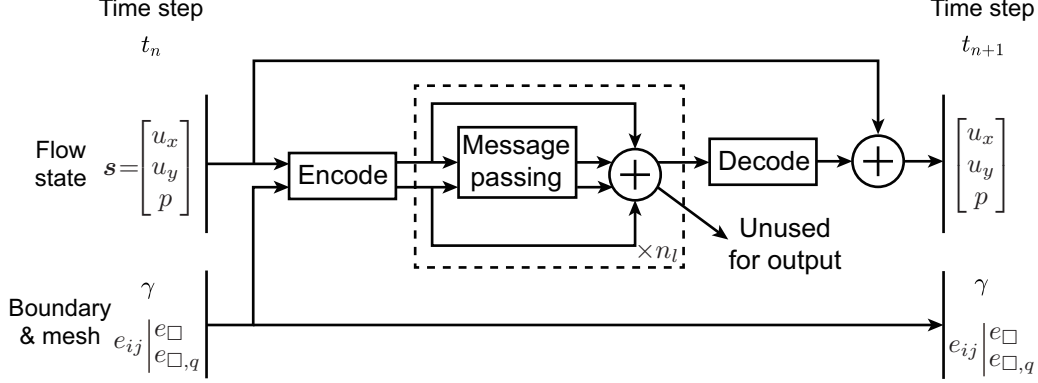


Figure 4: Schematic of the model architecture. The inputs at a time step  $t_n$  are the node features which contain the flow state  $s = [u_x, u_y, p]$  as well as boundary conditions  $\gamma$ , as well as the edge or element features which contain the mesh information. These inputs are first encoded, then pass through  $n_l = 15$  message-passing layers (marked out by the dashed box), and eventually the node features are decoded to generate the neural network output. As the flow state vector is completely attached to the nodes, the edge or element features are disposed after the last message-passing layer. Residual links are used for the node and edge/element features for the message-passing layers.

in which  $N_b$  is the total number of training steps within each epoch. We further stabilize the process by preventing  $\beta$  from increasing, i.e.,

$$\beta^2 \leftarrow (1 - \frac{1}{N_b})\beta^2 + \frac{1}{N_b} \min\{\beta^2, \text{MSE}(\psi_{batch} - \hat{\psi}_{batch})\} \quad (8)$$

for each training step.

## 4 Experiments

In this section, we apply the network described in Eq. 3 to the modeling and prediction of two fluid systems. In the subsequent subsections, we will first briefly describe the data sets used, then discuss the setup and training of the proposed and baseline models, and finally present the results. All experiments are performed with random seeds fixed at 1.

### 4.1 Experimental setup

**Data sets** We choose two typical fluid flow systems for the experiments: The flow around a circular cylinder and the flow around a NACA0012 airfoil. The flow around the cylinder is simulated at Reynolds number  $Re = 200$ , and used to test the capability of the neural network in learning a certain dynamic without overfitting it. The flow around the airfoil is simulated at multiple Reynolds numbers (with the flow at each Reynolds number forming a separate "trajectory") within the range  $Re \in [1000, 4000]$ , and used to test the capability of the network to interpolate within a range of dynamics and extrapolate out of the range. Both flow data sets are generated via a finite element solver written in Matlab. The simulated flow data are interpolated onto a coarser mesh before subsequent conversion to graph and hypergraph. More details on the data sets used are provided in appendix A.

**Models & implementation** We choose the state-of-the-art MeshGraphNet [6] as our baseline model, which applies a generalized message-passing network (Eq. 1) to the graph converted from mesh following Fig. 1b. Apart from the baseline, the performance of five models are evaluated and reported herein: The alternative MeshGraphNet with activation function changed to a sine function (abbreviated as *Node-edge-sin*), the node-element hypergraph message-passing networks with ReLU-like activation function (*Node-elem-A* and *Node-elem-B* for the node update stages defined by Eq. 3b and Eq. 3c respectively), and the node-element hypergraph message-passing networks with sinusoidal activation function (*Node-elem-A-sin* and *Node-elem-B-sin* for the node update stages defined by Eq. 3b and Eq. 3c respectively). All models are implemented in PyTorch [29]. The message-passing layers are implemented through a gather-scatter scheme similar to that in PyTorch Geometric [23]. Different from the practice in the original MeshGraphNet implementation, we follow the adaptation suggested by Lino et al. [11] to temporally evolve the pressure along with the velocity.

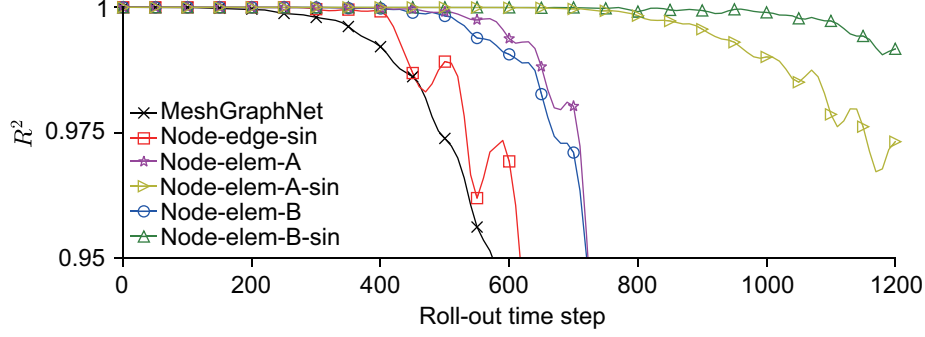


Figure 5: Coefficient of determination  $R^2$  of the predicted pressure field over 1200 steps for the flow around cylinder data set.

**Training** We train all models with Adam [30] optimizer for a total of 200 epochs with batch size 4. Following the practice in the MeshGraphNet baseline, MSE loss is used when ReLU-like activation functions are used. For models with sinusoidal activation function, adaptive smooth  $L_1$  loss described in Sec. 3.5 is used. It should be emphasized that we choose to NOT consider any training noise for all the cases reported. This is because the use of training noise would incur a significant computational cost in the process of tuning the hyperparameter for a fair assessment, as each architecture has its inherent compatibility for different types of training noises.

Further implementation and training details are provided in the appendix B. The code and data sets are publicly available at <https://github.com/garrygale/NodeElementMessagePassing>.

## 4.2 Evaluation metric

The trained models are evaluated on the test data sets. It should be noted that no cross-validation data sets are needed as we do not tune the hyperparameters, but rather follow the choices of the MeshGraphNet baseline. As the main purpose of the neural network surrogate model is to generate accurate roll-out simulations, we evaluate the models by feeding the state of the system at a certain time step, i.e. the first time step within each of the test data sets, to the model and compare the predicted system states over the next hundreds of time steps with the ground truth. Specifically, we quantitatively compare the similarity between the ground truth non-dimensionalized pressure field  $\mathbf{p}^*$  and its neural network prediction  $\hat{\mathbf{p}}^*$  over the prediction roll-out time steps by calculating the coefficient of determination

$$R^2 = 1 - \frac{\|\mathbf{p}^* - \hat{\mathbf{p}}^*\|_2^2}{\overline{\|\mathbf{p}^* - \mathbf{p}^*\|_2^2}}, \quad (9)$$

in which the overline  $\overline{(\cdot)}$  denotes the mean operation. A higher coefficient of determination indicates a more accurate prediction, up to  $R^2 = 1$  which means perfectly accurate predictions.

## 4.3 Results and discussion

Starting from the first time step in each of the test data sets, the models generate roll-out predictions of the states of the fluid systems over the future time steps. For the flow around cylinder data set, predictions for 1200 future time steps are generated. For the flow around airfoil data set, predictions for 800 future time steps are generated for each Reynolds number. In this subsection, we report these evaluation results, using the metric described in Sec. 4.2.

**Learning a certain flow dynamic** Figure 5 shows the coefficient of determination of the predicted non-dimensionalized pressure field  $\mathbf{p}^*$  for the flow around cylinder data set. It is clear that the node-element hypergraph message-passing networks are able to produce stable and accurate predictions for a longer period of time compared to the baseline MeshGraphNet. The use of the sinusoidal activation function proves to be helpful for the node-element hypergraph message-passing networks, verifying the hypothesis in Sec. 3.4. In the meantime, we notice that the improvement is way less pronounced when the sinusoidal activation function is used for the generalized message-passing network on a normal graph. As the training MSE error for both architectures reaches the order of  $1 \times 10^{-8}$  when the sinusoidal activation function is used, we conclude that the generalized message-passing network on a normal graph is more prone to overfitting when used to learn a certain flow dynamics.

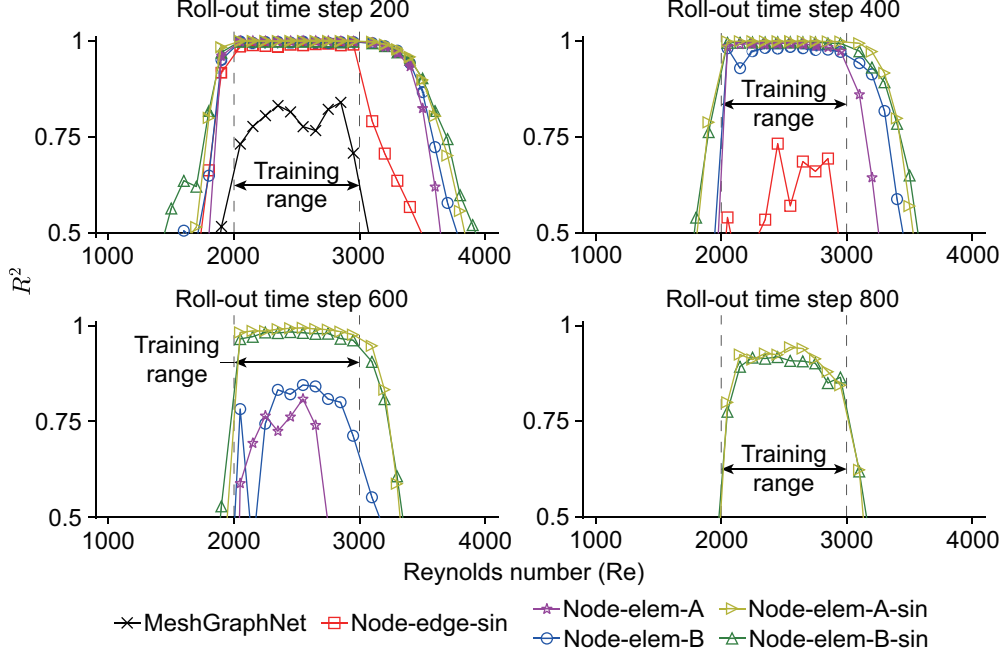


Figure 6: Coefficient of determination  $R^2$  of the predicted pressure field over the prediction roll-out for the flow around airfoil data set for all testing Reynolds numbers, sampled at roll-out time step 200, 400, 600, and 800.

**Interpolation & extrapolation** Figure 6 shows the coefficient of determination of the predicted non-dimensionalized pressure field  $\hat{p}^*$  for the flow around airfoil data sets at different Reynolds numbers. Note that the flow at each testing Reynolds number (i.e., each testing trajectory) is tested separately, using the system state of the first time step of each testing trajectory as the input to the model. The Reynolds number range of the training trajectories is marked out. Within the interpolation range, we observe that the node-element hypergraph message-passing networks are able to generate accurate roll-out predictions for a significantly longer period of time.

In the meantime, all models do not perform well in extrapolating out of the training Reynolds number range. This is within expectation, especially for MeshGraphNet, since all of its components are linear or piecewise linear functions, which means that the network output  $\hat{\psi}$  is a piecewise linear function of its inputs. Empirical results like reference [31] show that this kind of network extrapolates linearly outside of the training range. Since the dynamics of a fluid flow system, governed by the Navier-Stokes equations, is not linear, the network is not expected to be able to extrapolate outside of the training Reynolds number range. The same conclusion is also approximately (and only approximately as Gaussian Error Linear Unit (GELU) [32] activation function is used) true for the *node-elem-A* and *node-elem-B* models. For models with sinusoidal activation functions, the extrapolation pattern is not completely clear, but the results in Fig. 6 show that they are also not able to extrapolate well.

**Inference speed** Theoretically, the computational complexity of the models in concern should be similar, as a generalized graph message-passing layer and a node-element hypergraph message-passing layer require about the same number of gather and scatter operations. The actual inference time cost per step for all cases during evaluation are reported in Table 1. The node-element hypergraph message-passing networks run slightly slower than the graph message-passing layers. For the network with node update stage defined in Eq. 3b, the additional computational overhead is probably caused by the number of MLP evaluations needed for node update stage. For the network with node update stage defined in Eq. 3c, this is probably due to the fact that there is a data copying step in the implementation of Eq. 3c that we found unnecessary in theory, but difficult to circumvent in practice. When using sinusoidal activation functions, the networks generally run slightly slower, probably due to the fact that the evaluation of sine function is slower than ReLU-like activation functions.



Table 1: Inference time per prediction roll-out step.

Data set	MeshGraphNet	Node-edge-sin	Node-elem-A	Node-elem-A -sin	Node-elem-B	Node-elem-B -sin
Cylinder	$\approx 13.3$ ms	$\approx 14.9$ ms	$\approx 14.1$ ms	$\approx 16.2$ ms	$\approx 14.3$ ms	$\approx 18.5$ ms
Airfoil	$\approx 14.2$ ms	$\approx 16.5$ ms	$\approx 14.6$ ms	$\approx 17.5$ ms	$\approx 14.8$ ms	$\approx 15.5$ ms

## 5 Conclusion

Targeting the simulations of fluid systems with GNN, we converted the computational mesh to a node-element hypergraph rather than a normal graph. We implemented a message-passing network on such a hypergraph and showed that the network is able to generate stable and accurate roll-out predictions for a longer period of time compared with the baseline defined on a normal graph. We further demonstrated that the use of a sinusoidal activation function is preferable compared with ReLU-like activation functions.

As the proposed network architecture only changes the graph connectivity and message-passing strategy at individual graph levels, it should be compatible after minor modifications with most existing techniques like multi-grid methods and physical invariance and equivariance embedding strategies that were originally built upon graph neural networks defined on a normal graph. This means that we have established a new, stronger baseline for future research efforts in mesh-based fluids simulations with GNN.

It should be mentioned again that the current model only takes inspiration from the graph connectivity of the finite element method during the assembly process of the local stiffness matrices and load vectors. However, it remains untouched whether it be possible to construct a network architecture that is strictly a neural network version of the finite element method, which requires a step further from this work and the work by Lienen and Günnemann [21] appears to be in that direction. This possibility will be investigated further in our future work.

## Acknowledgment

This research is funded by the Natural Sciences and Engineering Research Council of Canada (NSERC) and Seaspan Shipyards. The training and evaluation of the neural network models were supported in part by the computational resources and services provided by Advanced Research Computing at the University of British Columbia. Dr. Renjie Liao and Xiaoyu Mao provided numerous suggestions to the work, their help is hereby gratefully acknowledged.

## References

- [1] Franco Scarselli, Marco Gori, Ah Chung Tsoi, Markus Hagenbuchner, and Gabriele Monfardini. The graph neural network model. *IEEE transactions on neural networks*, 20(1):61–80, 2008.
- [2] Jie Zhou, Ganqu Cui, Shengding Hu, Zhengyan Zhang, Cheng Yang, Zhiyuan Liu, Lifeng Wang, Changcheng Li, and Maosong Sun. Graph neural networks: A review of methods and applications. *AI Open*, 1:57–81, 2020.
- [3] Zonghan Wu, Shirui Pan, Fengwen Chen, Guodong Long, Chengqi Zhang, and S Yu Philip. A comprehensive survey on graph neural networks. *IEEE transactions on neural networks and learning systems*, 32(1):4–24, 2020.
- [4] Peter W Battaglia, Jessica B Hamrick, Victor Bapst, Alvaro Sanchez-Gonzalez, Vinicius Zambaldi, Mateusz Malinowski, Andrea Tacchetti, David Raposo, Adam Santoro, Ryan Faulkner, et al. Relational inductive biases, deep learning, and graph networks. *arXiv preprint arXiv:1806.01261*, 2018.
- [5] Filipe De Avila Belbute-Peres, Thomas Economou, and Zico Kolter. Combining differentiable pde solvers and graph neural networks for fluid flow prediction. In *international conference on machine learning*, pages 2402–2411. PMLR, 2020.
- [6] Tobias Pfaff, Meire Fortunato, Alvaro Sanchez-Gonzalez, and Peter W Battaglia. Learning mesh-based simulation with graph networks. *arXiv preprint arXiv:2010.03409*, 2020.
- [7] Roberto Perera, Davide Guzzetti, and Vinamra Agrawal. Graph neural networks for simulating crack coalescence and propagation in brittle materials. *Computer Methods in Applied Mechanics and Engineering*, 395:115021, 2022.
- [8] Tianju Xue, Sigrid Adriaenssens, and Sheng Mao. Learning the nonlinear dynamics of soft mechanical metamaterials with graph networks. *arXiv preprint arXiv:2202.13775*, 2022.

- [9] Marco Maurizi, Chao Gao, and Filippo Berto. Predicting stress, strain and deformation fields in materials and structures with graph neural networks. *Scientific Reports*, 12(1):1–12, 2022.
- [10] Jiayang Xu, Aniruddhe Pradhan, and Karthikeyan Duraisamy. Conditionally parameterized, discretization-aware neural networks for mesh-based modeling of physical systems. *Advances in Neural Information Processing Systems*, 34:1634–1645, 2021.
- [11] Mario Lino, Stathi Fotiadis, Anil A Bharath, and Chris D Cantwell. Multi-scale rotation-equivariant graph neural networks for unsteady eulerian fluid dynamics. *Physics of Fluids*, 34(8):087110, 2022.
- [12] Zhishuang Yang, Yidao Dong, Xiaogang Deng, and Laiping Zhang. Amgnet: multi-scale graph neural networks for flow field prediction. *Connection Science*, 34(1):2500–2519, 2022.
- [13] Rui Gao and Rajeev K Jaiman. Quasi-monolithic graph neural network for fluid-structure interaction. *arXiv preprint arXiv:2210.04193*, 2022.
- [14] Alvaro Sanchez-Gonzalez, Nicolas Heess, Jost Tobias Springenberg, Josh Merel, Martin Riedmiller, Raia Hadsell, and Peter Battaglia. Graph networks as learnable physics engines for inference and control. In *International Conference on Machine Learning*, pages 4470–4479. PMLR, 2018.
- [15] Peter Battaglia, Razvan Pascanu, Matthew Lai, Danilo Jimenez Rezende, et al. Interaction networks for learning about objects, relations and physics. *Advances in neural information processing systems*, 29, 2016.
- [16] Yunzhu Li, Jiajun Wu, Russ Tedrake, Joshua B Tenenbaum, and Antonio Torralba. Learning particle dynamics for manipulating rigid bodies, deformable objects, and fluids. *arXiv preprint arXiv:1810.01566*, 2018.
- [17] Meire Fortunato, Tobias Pfaff, Peter Wirsberger, Alexander Pritzel, and Peter Battaglia. Multiscale meshgraphnets. *arXiv preprint arXiv:2210.00612*, 2022.
- [18] Yadi Cao, Menglei Chai, Minchen Li, and Chenfanfu Jiang. Bi-stride multi-scale graph neural network for mesh-based physical simulation. *arXiv preprint arXiv:2210.02573*, 2022.
- [19] Ferran Alet, Adarsh Keshav Jeewajee, Maria Bauza Villalonga, Alberto Rodriguez, Tomas Lozano-Perez, and Leslie Kaelbling. Graph element networks: adaptive, structured computation and memory. In *International Conference on Machine Learning*, pages 212–222. PMLR, 2019.
- [20] Han Gao, Matthew J Zahr, and Jian-Xun Wang. Physics-informed graph neural galerkin networks: A unified framework for solving pde-governed forward and inverse problems. *Computer Methods in Applied Mechanics and Engineering*, 390:114502, 2022.
- [21] Marten Lienen and Stephan Günnemann. Learning the dynamics of physical systems from sparse observations with finite element networks. *arXiv preprint arXiv:2203.08852*, 2022.
- [22] Zhan Ma, Zisheng Ye, and Wenxiao Pan. Fast simulation of particulate suspensions enabled by graph neural network. *Computer Methods in Applied Mechanics and Engineering*, 400:115496, 2022.
- [23] Matthias Fey and Jan E Lenssen. Fast graph representation learning with PyTorch Geometric. In *ICLR Workshop on Representation Learning on Graphs and Manifolds*, 2019.
- [24] Vincent Sitzmann, Julien Martel, Alexander Bergman, David Lindell, and Gordon Wetzstein. Implicit neural representations with periodic activation functions. *Advances in Neural Information Processing Systems*, 33:7462–7473, 2020.
- [25] Ross Girshick. Fast r-cnn. In *Proceedings of the IEEE international conference on computer vision*, pages 1440–1448, 2015.
- [26] Cheng-Yang Fu, Mykhailo Shvets, and Alexander C Berg. Retinamask: Learning to predict masks improves state-of-the-art single-shot detection for free. *arXiv preprint arXiv:1901.03353*, 2019.
- [27] Hongkai Zhang, Hong Chang, Bingpeng Ma, Naiyan Wang, and Xilin Chen. Dynamic r-cnn: Towards high quality object detection via dynamic training. In *European conference on computer vision*, pages 260–275. Springer, 2020.
- [28] Arief Rachman Sutanto and Dae-Ki Kang. A novel diminish smooth l1 loss model with generative adversarial network. In *International Conference on Intelligent Human Computer Interaction*, pages 361–368. Springer, 2021.
- [29] Adam Paszke, Sam Gross, Francisco Massa, Adam Lerer, James Bradbury, Gregory Chanan, Trevor Killeen, Zeming Lin, Natalia Gimelshein, Luca Antiga, et al. Pytorch: An imperative style, high-performance deep learning library. *Advances in neural information processing systems*, 32, 2019.
- [30] Diederik P Kingma and Jimmy Ba. Adam: A method for stochastic optimization. *arXiv preprint arXiv:1412.6980*, 2014.

- [31] Keyulu Xu, Mozhi Zhang, Jingling Li, Simon S Du, Ken-ichi Kawarabayashi, and Stefanie Jegelka. How neural networks extrapolate: From feedforward to graph neural networks. *arXiv preprint arXiv:2009.11848*, 2020.
- [32] Dan Hendrycks and Kevin Gimpel. Gaussian error linear units (gelus). *arXiv preprint arXiv:1606.08415*, 2016.
- [33] Christophe Geuzaine and Jean-François Remacle. Gmsh: A 3-d finite element mesh generator with built-in pre-and post-processing facilities. *International journal for numerical methods in engineering*, 79(11):1309–1331, 2009.
- [34] Rajeev K Jaiman, M Z Guan, and Tharindu P Miyanawala. Partitioned iterative and dynamic subgrid-scale methods for freely vibrating square-section structures at subcritical reynolds number. *Computers & Fluids*, 133:68–89, 2016.
- [35] Pauli Virtanen, Ralf Gommers, Travis E Oliphant, Matt Haberland, Tyler Reddy, David Cournapeau, Evgeni Burovski, Pearu Peterson, Warren Weckesser, Jonathan Bright, Stéfan J van der Walt, Matthew Brett, Joshua Wilson, K Jarrod Millman, Nikolay Mayorov, Andrew R J Nelson, Eric Jones, Robert Kern, Eric Larson, C J Carey, İlhan Polat, Yu Feng, Eric W Moore, Jake VanderPlas, Denis Laxalde, Josef Perktold, Robert Cimrman, Ian Henriksen, E A Quintero, Charles R Harris, Anne M Archibald, Antônio H Ribeiro, Fabian Pedregosa, Paul van Mulbregt, and SciPy 1.0 Contributors. SciPy 1.0: Fundamental Algorithms for Scientific Computing in Python. *Nature Methods*, 17:261–272, 2020.
- [36] Jimmy Lei Ba, Jamie Ryan Kiros, and Geoffrey E Hinton. Layer normalization. *arXiv preprint arXiv:1607.06450*, 2016.

## A Details of the data sets used

Two data sets are used for the evaluation of the model. In this appendix, we provide the detailed description of these data sets.

### A.1 Data generation and train-test split

Both flow data sets are 2-D incompressible fluid flow simulated at laminar flow conditions. The computational meshes are created with Gmsh [33]. The momentum equations are solved using a Petrov-Galerkin finite element solver with a semi-discrete time-stepping scheme [34] written in Matlab. The domain for the two sets of simulations is plotted in Fig. 7. The inlet features a uniform flow  $u_x = U_\infty = 1$ ,  $u_y = 0$  condition, the outlet  $\Gamma_{out}$  is set to be traction free, while top and bottom of the boundary conditions  $\Gamma_{top}$  and  $\Gamma_{bottom}$  are set to be slip-wall. The computational meshes are shown in Fig. 8a and Fig. 9a. For the flow around cylinder, a total of 6499 continuous time steps are sampled with non-dimensionalized time step  $\Delta t^* = 0.04$  at Reynolds number  $Re = 200$ . For the flow around an airfoil, the data are sampled at 61 different Reynolds numbers within the range  $Re \in [1000, 4000]$ . For each of the considered Reynolds number, 4500 continuous time steps are sampled with non-dimensionalized time step  $\Delta t^* = 0.0167$ .

For the neural network, we use coarser meshes for both cases, depicted in Fig. 8b and 9b. It should be noted that the meshes for the flow around cylinder are the same as the one used for the fluid-structure interaction between fluid flow and an elastically mounted cylinder in reference [13]. The statistics about the number of nodes, edges and elements for the two data sets are reported in Table 2. The simulated flow data on the dense CFD mesh are interpolated onto the coarse neural network mesh via a clough-tocher interpolator available in SciPy package [35].

Table 2: Statistics of the converted graph/hypergraph for the data sets used

Data set	Nodes	Edges	Elements	Element-node edges
Cylinder	2204	8728	2160	8640
Airfoil	3653	14486	3590	14360

The interpolated data sets are then split into train and test data sets, as listed in Table 3. Separate cross-validation data sets are not necessary, since we do not fine-tune the hyperparameters of the model, but rather follow the choices in the MeshGraphNet baseline [6].

### A.2 Graph feature attachment

After being interpolated onto the coarser mesh, the flow data are then converted and re-attached to the graph and hypergraph that are converted from the coarse mesh (cf. Fig. 1 and 2). As the two data sets used in this work are both

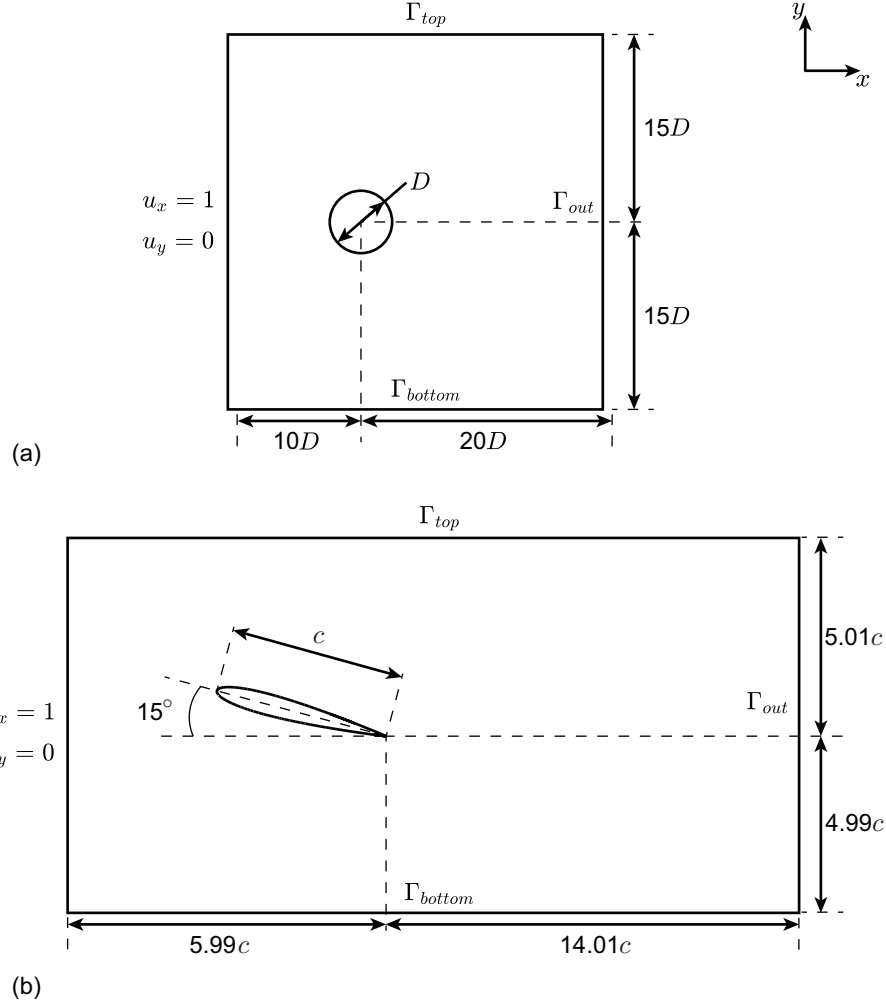


Figure 7: Schematic of the computational domain for the two data sets. Flow around (a) a circular cylinder (b) a NACA0012 airfoil at 15 degrees angle of attack.

Table 3: Train-test split of the data sets. The  $a : b : c$  notation denotes a series of values starting from  $a$  and ends at  $c$ , with interval  $b$  and both ends included.

Data set	Training Reynolds number(s)	Testing Reynolds number(s)	Time steps per training trajectory	Time steps per testing trajectory
Cylinder	200	200	2048	1200
Airfoil	2000: $\frac{100}{3}$ : 3000	1000:100:1900 2050:100:2950 3100:100:4000	512	800

fluid flow data sets, they share the same feature attachment procedure. For features on the normal graph, the node features are the velocity  $(u_x, u_y)$  and pressure  $p$ , as well as the boundary condition  $\gamma$  (encoded as a one-hot vector):

$$v_i = [u_{x,i}, u_{y,i}, p_i, \gamma_i], \quad (10)$$

The edge features encode the relative location information

$$e_{ij} = [x_i - x_j, y_i - y_j, \sqrt{(x_i - x_j)^2 + (y_i - y_j)^2}], \quad (11)$$

for a directed edge pointing from node  $i$  at spatial coordinate  $(x_i, y_i)$  to node  $j$  at  $(x_j, y_j)$ .

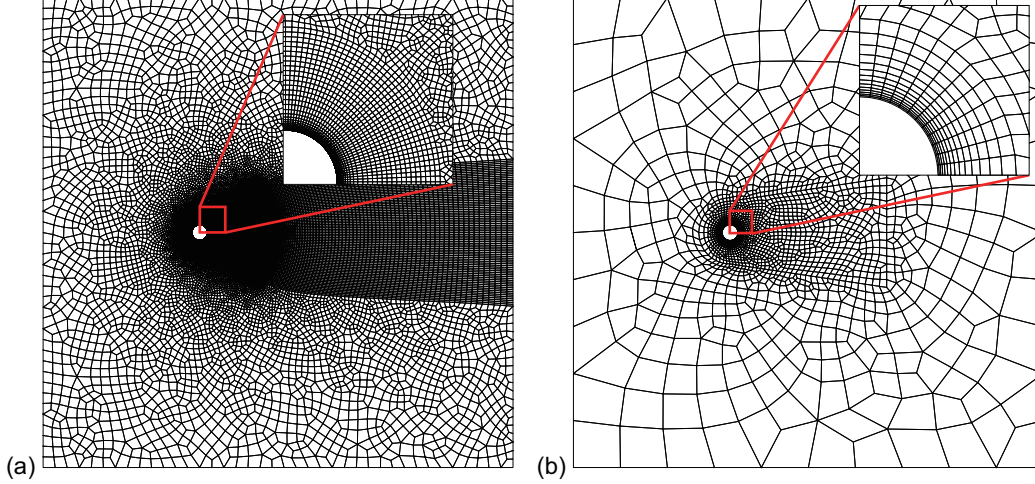


Figure 8: Schematic of the mesh used for the flow around cylinder case. (a) Computational mesh for the CFD solver. (b) Coarser mesh to be converted to graph and hypergraph for neural network.

For the node-element hypergraph, the node features are the same as that of the normal graph. The features on the element-node edges are used to encode the relative location information. For an element connecting four nodes  $i, j, k$ , and  $l$ , the element-node features are chosen to be

$$e_{\square, p} = [x_p - \bar{x}_p, y_p - \bar{y}_p] \quad (12)$$

for  $p = i, j, k, l$ . The feature on each element encodes the area of the corresponding cell  $S_{\square}$ ,

$$e_{\square} = [S_{\square}, -S_{\square}] \quad (13)$$

To avoid a feature vector of length 1, we augment the element feature vector by concatenating it with its negative vector.

The feature vectors are normalized before being used for training. The edge or element feature vectors are normalized to zero mean and unit standard deviation entry-by-entry (i.e., normalized in the graph and sample dimensions, but not in the feature dimension). For models with ReLU-like activation functions, the system state part of the node feature vectors (i.e.,  $u_x, u_y$  and  $p$ ) are normalized to zero mean and unit standard deviation entry-by-entry, while the boundary one-hot vectors are not normalized. For models with sinusoidal activation function, the system state part of the node feature vectors gone through a min-max normalization with minimum  $-1$  and maximum  $1$  entry-by-entry. The targets of the models  $\psi_n = s_{n+1} - s_n$  are calculated after the normalization, and then normalized again using the same strategy.

## B Implementation and training

We use PyTorch [29] to implement all the models. In all reported message-passing models, all MLPs (encoder, decoder and the nonlinear functions in the message-passing layers) have two hidden layers with layer width 128 except for the outputs of the decoders which have size 3. A total of 15 message-passing layers are used for all reported models. Residual links are added for all message-passing layers. The mean aggregation function is used for all element update stages. The sum aggregation function is used for the models with ReLU-like activation functions, while the mean aggregation function is used for models with sinusoidal activation functions. In order to improve convergence, layer normalization [36] is added at the end of all MLPs (except for decoders) for models with ReLU-like activation functions. All the trainings are performed with all random seeds fixed at 1 and batch size 4, using an Adam [30] optimizer with PyTorch default setup, and lasts for 200 epochs. The detailed learning rate scheme is reported in Table 4. All training and evaluation runs are completed on a single Nvidia RTX 3090 GPU with CPU being AMD Ryzen 9 5900 @ 3 GHz  $\times$  12 cores.

For the MeshGraphNet baseline, we translate from the TensorFlow implementation provided by Pfaff et al. [6]. It should be noted that our implementation is different from the original version in that:

1. We no longer gather normalization statistics (mean and standard deviations of inputs and outputs) on-the-fly, but rather use the whole training data set to directly calculate them in the pre-processing stage.

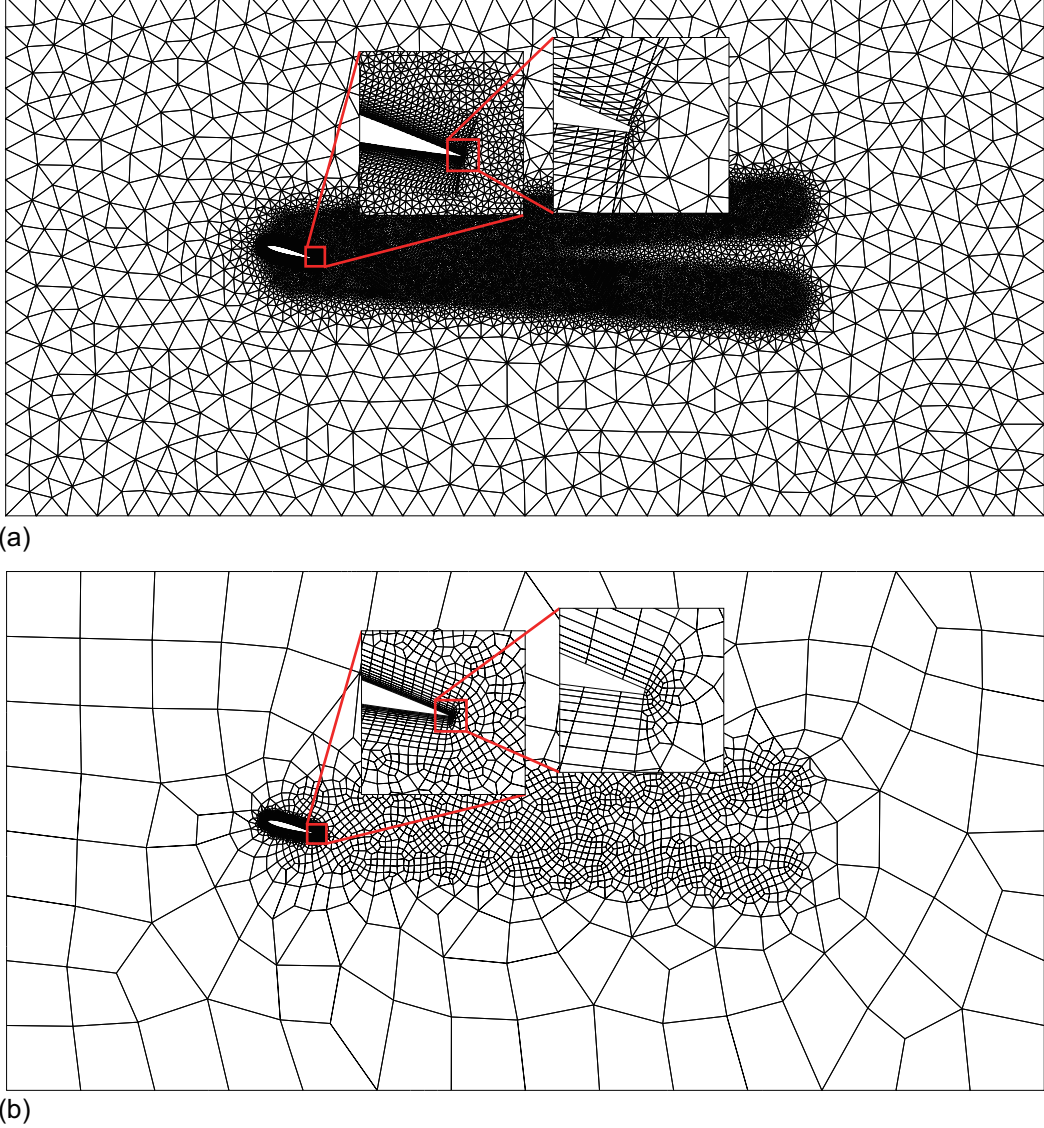


Figure 9: Schematic of the mesh used for the flow around airfoil case. (a) Computational mesh for the CFD solver. (b) Coarser mesh to be converted to graph and hypergraph for the graph neural network.

2. We adopt the modification suggested by Lino et al. [11] to also include pressure in the temporal roll-out, in addition to the velocity. Due to this modification, the outputs of the neural network at the domain boundaries are now included in the calculation of loss, and used in the prediction temporal roll-out.
3. The results reported are generated from models trained without the use of training noise. This is because we notice that the optimal amount of training noise varies with the data sets, networks, and training noise schemes used, leading to hyper-parameters that are too computationally expensive to tune for a fair comparison.
4. The learning rate scheme is slightly different from the original implementation. We add a learning rate warm-up stage of 10 epochs, and the learning rate does not decay immediately from the start. The max learning rate ( $10^{-4}$ ) and min learning rate ( $10^{-6}$ ) are kept the same as the original implementation. We also apply the same training scheme for other reported models.

For the node-element message-passing with ReLU-like activation functions, we use Gaussian Error Linear Units (GELU) [32] activation function rather than ReLU in the MeshGraphNet baseline. This is because MeshGraphNet generates better results with ReLU compared to GELU, while the reverse is true for node-element hypergraph message-passing

Table 4: Neural network training scheme

Stage	Batch size	Epochs	Starting learning rate	Ending learning rate	Learning rate change
1	4	10	$10^{-6}$	$10^{-4}$	Linear, per step
2		40	$10^{-4}$	$10^{-4}$	N/A
3		100	$10^{-4}$	$10^{-6}$	Exponential, per epoch
4		50	$10^{-6}$	$10^{-6}$	N/A

networks. For the message-passing networks with sinusoidal activation function, we consider the sine activation function [24] along with the specific initialization schemes described in the work.

The message-passing layers are implemented in a gather-scatter scheme, which is rather similar to that in PyTorch Geometric [23] but not exactly the same. Due to the use of the GPU atomic operation in the scatter functions, the training and evaluation processes are not deterministic even when all random numbers are fixed, and some differences are expected between the network parameters obtained from running the provided code and the trained network parameters provided.